PHYSICAL REVIEW E **91**, 023305 (2015)

Improved forcing scheme in pseudopotential lattice Boltzmann methods for multiphase flow at arbitrarily high density ratios

Daniel Lycett-Brown and Kai H. Luo
Department of Mechanical Engineering, University College London, Torrington Place, London WC1E 7JE, United Kingdom
(Received 16 September 2014; revised manuscript received 19 December 2014; published 11 February 2015)

The pseudopotential lattice Boltzmann method has been widely used to simulate many multiphase flow applications. However, there still exist problems with reproducing realistic values of density ratio and surface tension. In this study, a higher-order analysis of a general forcing term is derived. A forcing scheme is then constructed for the pseudopotential method that is able to accurately reproduce the full range of coexistence curves. As a result, multiphase flow of arbitrarily high density ratios independent of the surface tension can be simulated. Furthermore, the interface width can be tuned to allow for grid refinement and systematic error reduction. Numerical results confirm that the proposed scheme enables independent control of density ratio, surface tension, and interface width simultaneously.

DOI: 10.1103/PhysRevE.91.023305 PACS number(s): 47.11.−j, 47.55.−t

I. INTRODUCTION

The lattice Boltzmann method (LBM) is a rapidly developing approach to computational fluid dynamics (CFD). It has been successfully applied to a variety of problems, including (but not limited to) turbulence, microflows, flows through porous media, magnetohydrodynamics, multiphase flow, and multicomponent systems (see, for example, Refs. [1–3] and references therein). Instead of solving the macroscopic Navier-Stokes equations as in traditional CFD, the LBM works on the mesoscopic scales, solving a discretized Boltzmann equation, designed to recover the Navier-Stokes equations in the macroscopic limit. Despite its success in many applications, there still exists a fundamental debate over the inclusion of a term in the lattice Boltzmann equation that will correctly recover a force in the Navier-Stokes equation. This is particularly significant when a forcing scheme is used to model multiphase behavior in the LBM. Here we propose a forcing scheme that correctly reproduces the multiphase coexistence curve at high density ratios and allows for accurate control over surface tension.

A number of methods for including multiphase behavior into the LBM have been proposed, including the free-energy models [4–6], those based on the kinetic theory of dense fluids [7–9], and the interaction potential models [10–12]. These methods can all be formulated in the form of an additional forcing term to the collision operator. While here the interaction potential model of Shan and Chen [10] is considered, the analysis has implications for each of these multiphase methods. It is well known that the original formulation of the Shan-Chen model is only stable for low liquid to gas phase density ratios, and over a small range of viscosities. Another significant problem is the formation of spurious velocities around curved interfaces. A number of improvements to the model have been proposed and can be divided into two categories: those that modify the force calculation, such as increasing the order of isotropy [13] or modifying the equation of state [14], and those that improve the incorporation of the force term into the equilibrium distribution functions. It is these latter modifications that are considered here. They include the method of explicit derivatives, as used in the multiphase schemes derived from the kinetic theory of dense fluids [7–9], the method of Guo *et al.* [15], which takes into account discrete lattice effects, and the exact difference method (EDM) [16].

It has been shown recently that while the method of Guo *et al.* [15] recovers the Navier-Stokes equations correctly, the EDM introduces an error into the pressure tensor, proportional to the square of the forcing term [15,17]. However, results show that the EDM is stable over a larger range of density ratios than the method of Guo *et al.* [15], and it gives smaller errors for high density ratio multiphase systems [16,18] when using the Carnahan-Starling equation of state. Conversely, the method of Guo *et al.* [15] preforms better than the EDM for the exponential form of the equation of state proposed by Shan and Chen. This has resulted in some confusion over which forcing scheme is the most appropriate to use. However, the analysis used is based on a second-order expansion of the LBM, which has been shown to be insufficient to identify all relevant error terms when considering forces with large gradients, as are present at interfaces in multiphase schemes [19]. Here we extended the third-order truncation error analysis of Holdych *et al.* [20] to include forcing terms in order to correctly identify the errors in the pressure tensor. It is well known that only one form of the equation of state is thermodynamically consistent in the interaction potential model. As the error terms under discussion affect the coexistence curve, it is possible for errors in the pressure tensor to counteract this lack of thermodynamical consistency. As will be shown, this effect can lead to some forcing schemes working better under certain circumstances, despite introducing larger errors.

The LBM with a generic forcing term and the derivation of the pressure tensor in the pseudopotential model are summarized in Sec. II. The extension of the third-order truncation analysis to include a generic forcing term is then given in Sec. III. The consequent correction to the surface tension and the addition of a term to control surface tension are discussed in Sec. IV. Results for the reproduction of coexistence curves in one dimension are given in Sec. V A, along with a study of the effect of varying model parameters on density ratio. Results for the two-dimensional case are then given in Secs. V B and V C, including surface tension measurements and the effect of varying surface tension and interface width on the spurious velocities found around curved

phase boundaries. Finally, a summary and outlook are given in Sec. VI.

II. THE LATTICE BOLTZMANN MODEL

The single relaxation time LBM with a general forcing term, F_i, is written as

$$f_i(\mathbf{x}+\mathbf{v}_i,t+1)-f_i(\mathbf{x},t)=-\frac{1}{\tau}\left(f_i-f_i^{\mathrm{eq}}\right)+F_i, \quad (1)$$

where f_i are particle distribution functions for particles with velocities $\mathbf{v}_i$, $\mathbf{x}$ and t are space and time coordinates, and τ is the relaxation time. The number of discrete velocities, Q, depends on the lattice, where the subscript $i=1,\ldots,Q$. The equilibrium distribution functions are given by

$$f_i^{\mathrm{eq}}=\rho w_i\left(1+\frac{\mathbf{v}_i\cdot\mathbf{u}}{T_0}+\frac{(\mathbf{v}_i\cdot\mathbf{u})^2}{2T_0^2}-\frac{\mathbf{u}^2}{2T_0}\right)+O(\mathbf{u}^3), \quad (2)$$

where T_0 is the (lattice dependent) reference temperature, and w_i are weights. The density, ρ, and macroscopic fluid velocity, $\mathbf{u}$, are found as velocity moments of the distribution functions,

$$\begin{aligned}\rho&=\sum_i f_i,\\ \rho\mathbf{u}&=\sum_i \mathbf{v}_i f_i.\end{aligned} \quad (3)$$

The second, third, and fourth moments are written as $\mathbf{\Pi}$, $\mathbf{Q}$, and $\mathbf{A}$, respectively. The form of F_i depends on the method, however the zeroth and first velocity moments must be

$$\begin{aligned}\sum_i F_i&=0,\\ \sum_i \mathbf{v}_i F_i&=\mathbf{F},\end{aligned} \quad (4)$$

where $\mathbf{F}$ is the force acting on the fluid. The general second and third moments of F_i are $\mathbf{\Psi}$ and $\mathbf{\Xi}$, respectively.

The derivation of the Navier-Stokes equation from the LBM is deferred to the following section, where the exact form of F_i will be discussed. For now we assume $\mathbf{F}$ is correctly introduced into the Navier-Stokes equation, and we consider the resulting pressure tensor when $\mathbf{F}$ has the form of a pseudopotential force. In the Shan-Chen model, this is given by

$$\mathbf{F}(\mathbf{x})=-Gc_s^2\psi(\mathbf{x})\sum_{i=1}^{N} w(|\mathbf{v}_i|^2)\psi(\mathbf{x}+\mathbf{v}_i)\mathbf{v}_i, \quad (5)$$

where ψ is the density-dependent interaction potential, G controls the strength of the interaction, $w(|\mathbf{v}_i|^2)$ are weights, and c_s is the speed of sound. The number of discrete velocities, N, used in the force calculation does not have to be equal to the number of lattice velocities. In general, weights are also different from those in the equilibrium distribution functions. The Taylor series expansion of $\psi(\mathbf{x}+\mathbf{v}_i)$ gives [8]

$$\mathbf{F}(\mathbf{x})=-Gc_s^2\psi\nabla\psi-\lambda Gc_s^2\psi\nabla(\Delta\psi), \quad (6)$$

where λ depends on N. Using this equation and the definition

$$\nabla\cdot\mathbf{P}=\nabla\left(\rho c_s^2\right)-\mathbf{F}, \quad (7)$$

the pressure tensor, $\mathbf{P}$, is given by

$$\mathbf{P}=\left(\rho c_s^2+G\frac{c_s^2}{2}\psi^2+Gc_s^2\frac{\lambda}{2}|\nabla\psi|^2+Gc_s^2\lambda\psi\Delta\psi\right)\mathbf{I}-Gc_s^2\lambda\nabla\psi\nabla\psi, \quad (8)$$

where $\mathbf{I}$ is the identity matrix. $\lambda=1/6$ for a two-dimensional lattice with nine velocities ($N=9$). An alternative derivation of the pressure tensor, originally proposed by Shan and Chen [11] and more recently extended by Shan [21], results in different coefficients in place of each λ in Eq. (8). The derivation is based on the discrete form of the integral of Eq. (8). However, based on results for coexistence curves in one dimension, as presented in Sec. V A, these coefficients are not correct, therefore this result is not discussed further here.

The mechanical stability condition is now considered, following Shan [21]. From Eq. (8), the pressure normal to a flat interface with gradients only in the x direction is given by

$$P_{xx}=\rho c_s^2+G\frac{c_s^2}{2}\psi^2+Gc_s^2a\left(\frac{\partial\psi}{\partial x}\right)^2+Gc_s^2b\psi\frac{\partial^2\psi}{\partial x^2}, \quad (9)$$

where a and b are given here by $a=-\lambda/2$ and $b=\lambda$. Setting this equal to the static pressure in the bulk, p_0, and integrating with respect to ρ (see, for example, Li *et al.* [22]), gives

$$\left(\frac{\partial\rho}{\partial x}\right)^2\Bigg|_{\rho_g}^{\rho_l}\propto\int_{\rho_g}^{\rho_l}\left(p_0-\rho c_s^2-G\frac{c_s^2}{2}\psi^2\right)\frac{1}{\psi^{1+\epsilon}}\frac{\partial\psi}{\partial\rho}d\rho, \quad (10)$$

where the subscripts l and g refer to the liquid and gas phase, respectively, and

$$\epsilon=-\frac{2a}{b}. \quad (11)$$

As $\partial\rho/\partial x=0$ in the bulk, then the liquid and gas densities must satisfy

$$\int_{\rho_g}^{\rho_l}\left(p_0-\rho c_s^2-G\frac{c_s^2}{2}\psi^2\right)\frac{1}{\psi^{1+\epsilon}}\frac{\partial\psi}{\partial\rho}d\rho=0. \quad (12)$$

From thermodynamic theory, the Maxwell construction gives [11]

$$\int_{\rho_g}^{\rho_l}\left(p_0-\rho c_s^2-G\frac{c_s^2}{2}\psi^2\right)\frac{1}{\rho^2}d\rho=0, \quad (13)$$

therefore for thermodynamic consistency it is required that [23]

$$\frac{1}{\psi^{1+\epsilon}}\frac{\partial\psi}{\partial\rho}\propto\frac{1}{\rho^2}. \quad (14)$$

Surface tension is defined as [24]

$$\sigma=\int_{-\infty}^{\infty}(P_{xx}-P_{yy})dx, \quad (15)$$

which from Eq. (8) is given by

$$\sigma=-Gc_s^2\lambda\int_{-\infty}^{\infty}\left|\frac{\partial\psi}{\partial x}\right|^2dx. \quad (16)$$

These expressions for the mechanical stability condition and surface tension assume that $\mathbf{F}$ is introduced into the Navier-Stokes equation without any error. As will be shown in the

following section, this is not the case. Before proceeding to identify these errors, it is important to note the following two relationships, derivable from Eq. (6):

$$\frac{\mathbf{FF}}{\rho} = G^2 c_s^4 \frac{\psi^2}{\rho} \nabla\psi\nabla\psi, \tag{17}$$

$$\frac{\partial F_\alpha}{\partial x_\beta} = -G c_s^2 \left[\psi \frac{\partial^2 \psi}{\partial x_\alpha \partial x_\beta} + \left(\frac{\partial \psi}{\partial x_\alpha}\right)\left(\frac{\partial \psi}{\partial x_\beta}\right)\right]. \tag{18}$$

Any errors in the pressure tensor proportional to **FF** or gradients of **F** will directly affect the mechanical stability condition and surface tension. The issue with the second-order expansion arises as the second-order derivatives in the pressure tensor are of higher order than the second order in the Navier-Stokes equations. To correctly identify the errors, the second-order Chapman-Enskog expansion often used in LBM analysis is therefore insufficient [19]. However, taking the expansion to higher order leads to Burnett level equations. As this is not the goal, only terms in F are needed from a third-order analysis, because F and its derivatives are large around phase boundaries. Here we proceed with a third-order analysis, following the work of Holdych *et al.* [20]. However, it should be noted that there is still debate over whether this method is equivalent to a Chapman-Enskog expansion, once they are taken beyond second order [19].

III. THIRD-ORDER TRUNCATION ERROR

The third-order analysis of the LBM with a general forcing term is now given. Equation (1) can be recast in the form

$$f_i(\mathbf{x},t) = \left(1-\frac{1}{\tau}\right) f_i(\mathbf{x}-\mathbf{v}_i,t-1) + \frac{1}{\tau} f_i^{\mathrm{eq}}(\mathbf{x}-\mathbf{v}_i,t-1) + F_i(\mathbf{x}-\mathbf{v}_i,t-1), \tag{19}$$

the recursive application of which can be used to eliminate the f_i dependence on the right-hand side, resulting in

$$f_i(\mathbf{x},t) = \frac{1}{\tau}\sum_{n=1}^{\infty}\left(1-\frac{1}{\tau}\right)^{n-1} f_i^{\mathrm{eq}}(\mathbf{x}-n\mathbf{v}_i,t-n) + \sum_{n=1}^{\infty}\left(1-\frac{1}{\tau}\right)^{n-1} F_i(\mathbf{x}-n\mathbf{v}_i,t-n). \tag{20}$$

Taylor expansions can then be used to give

$$f_i(\mathbf{x},t) = f_i^{\mathrm{eq}}(\mathbf{x},t) + \frac{1}{\tau}\sum_{n=1}^{\infty}\sum_{m=1}^{\infty}\left(1-\frac{1}{\tau}\right)^{n-1} \times \frac{(-n)^m}{m!}\left(\frac{\partial}{\partial t}+\mathbf{v}_i\cdot\nabla\right)^m f_i^{\mathrm{eq}}(\mathbf{x},t) + \tau F_i(\mathbf{x},t) + \sum_{n=1}^{\infty}\sum_{m=1}^{\infty}\left(1-\frac{1}{\tau}\right)^{n-1} \times \frac{(-n)^m}{m!}\left(\frac{\partial}{\partial t}+\mathbf{v}_i\cdot\nabla\right)^m F_i(\mathbf{x},t). \tag{21}$$

Keeping terms up to third derivatives, the zeroth and first velocity moments of this equation are then taken. Moments of the equilibrium distribution are denoted with superscript 0. The resulting equations for ρ and $\rho\mathbf{u}$ can then be used to derive the conservation of mass and momentum by recursively eliminating derivatives of these terms. Full details are given in the Appendix. The conservation of mass is given by the familiar form

$$\frac{\partial \rho}{\partial t} + \nabla\cdot(\rho\hat{\mathbf{u}}) = 0, \tag{22}$$

where as usual the fluid velocity $\mathbf{u}$ has been modified as

$$\rho\mathbf{u} = \rho\hat{\mathbf{u}} - \mathbf{F}/2 \tag{23}$$

(third derivatives have been dropped here, however including them in the definition of $\hat{\mathbf{u}}$ does not change the final result). The conservation of momentum gives

$$\frac{\partial}{\partial t}(\rho\hat{\mathbf{u}}) + \nabla\left(c_s^2\rho\right) + \nabla\cdot(\rho\hat{\mathbf{u}}\hat{\mathbf{u}}) = \nabla\cdot\boldsymbol{\tau} + \mathbf{F} + \nabla\cdot\left[\left(\tau-\frac{1}{4}-\tau\gamma\right)\frac{\mathbf{FF}}{\rho}\right] + \nabla\cdot\left[\frac{T_0}{12}[(\nabla\cdot\mathbf{F})\mathbf{I} + \nabla\mathbf{F} + (\nabla\mathbf{F})^{\mathrm{T}}]\right], \tag{24}$$

where the deviatoric stress tensor is given in the usual form for the single relaxation time LBM as

$$\boldsymbol{\tau} = T_0\left(\tau-\tfrac{1}{2}\right)\rho[\nabla\hat{\mathbf{u}} + (\nabla\hat{\mathbf{u}})^{\mathrm{T}}]. \tag{25}$$

The last two terms in Eq. (24) are errors in the Navier-Stokes equation. These errors are general and will apply to any force. In the case of a small external force, they will have little effect, but they should be taken into account for any force with large gradients. This includes all multiphase methods that can be arranged into the form of Eq. (1). Here, however, we consider the case in which the force is given specifically by Eq. (5). Using Eqs. (17) and (18), the pressure tensor with the resulting errors is then given by

$$\mathbf{P} = \left[\rho c_s^2 + G\frac{c_s^2}{2}\psi^2 + G c_s^2\left(\frac{c_s^2}{12}+\frac{\lambda}{2}\right)|\nabla\psi|^2 + G c_s^2\left(\frac{c_s^2}{12}+\lambda\right)\psi\boldsymbol{\Delta}\psi\right]\mathbf{I} + G c_s^2\left[\frac{c_s^2}{6} - \lambda - G c_s^2\left(\tau-\frac{1}{4}-\tau\gamma\right)\frac{\psi^2}{\rho}\right]\nabla\psi\nabla\psi + \frac{G c_s^4}{6}\psi\nabla\nabla\psi, \tag{26}$$

where $T_0 = c_s^2$ has been used. The importance of the terms from the third-order expansion is immediately obvious. We first consider the impact on the mechanical stability condition, and we leave the discussion of surface tension to the following section. The pressure normal to a flat interface with gradients only in the x direction is now given by

$$P_{xx} = \rho c_s^2 + G\frac{c_s^2}{2}\psi^2 + G c_s^2\left[\frac{c_s^2}{4} - \frac{\lambda}{2} - \left(\tau-\frac{1}{4}-\tau\gamma\right)G c_s^2\frac{\psi^2}{\rho}\right]\left(\frac{\partial\psi}{\partial x}\right)^2 + G c_s^2\left[\frac{c_s^2}{4}+\lambda\right]\psi\frac{\partial^2\psi}{\partial x^2}. \tag{27}$$

With the error terms included, the coefficients a and b in Eq. (9), corresponding to the first and second terms in square brackets in Eq. (27), have been changed. Consequently, ϵ is now given by

$$\epsilon = -2\frac{\frac{c_s^2}{4} - \frac{\lambda}{2} - \left(\tau - \frac{1}{4} - \tau\gamma\right) G c_s^2 \frac{\psi^2}{\rho}}{\frac{c_s^2}{4} + \lambda}. \tag{28}$$

From Eq. (12) it can be seen that these errors effect the mechanical stability condition. This is the reason that previous methods have not been able to correctly reproduce the coexistence curve. However, some success has been achieved, with different forcing schemes working better with different equations of state. This has led to confusion over which of the existing forcing schemes is correct. All existing forcing schemes can be rearranged into the form of Eq. (1), therefore γ can then be derived. It is well known that the original forcing scheme in the Shan-Chen method gave liquid and gas densities dependent on τ; this is due to a τ^2 term appearing in γ. The exact difference method has

$$\gamma_{\mathrm{EDM}} = 1. \tag{29}$$

This cancels the τ dependence in Eq. (28) (the Shan-Chen method coincides with the EDM at $\tau = 1$). The method of Guo *et al.* [15] has

$$\gamma_{\mathrm{Guo}} = 1 - 1/4\tau, \tag{30}$$

and this removes both the τ and ψ^2/ρ dependencies in ϵ. For the specific case of the two-dimensional, nine velocity lattice, $\lambda = 1/6$, and therefore using this method, $\epsilon = 0$. Solving Eq. (14) for thermodynamic consistency with $\epsilon = 0$ gives

$$\psi \propto \exp\left(-\frac{1}{\rho}\right). \tag{31}$$

This form for the pseudopotential is common in the literature, however it must be stressed that without the coincidental cancellation between the lattice-dependent value of λ and the error term, the method of Guo would not give the correct coexistence curve. If a different lattice is used, where $\lambda \neq 1/6$, then $\epsilon \neq 0$, and the coexistence curve will be incorrect. More realistic equations of state can be used by choosing ψ to be [14]

$$\psi = \sqrt{\frac{2\left(p_0 - \rho c_s^2\right)}{G c_s^2}}, \tag{32}$$

and setting p_0 to the desired equation of state. For example, the Carnahan-Starling equation of state is given by

$$p_0 = \rho R T \frac{1 + \frac{\beta\rho}{4} + \left(\frac{\beta\rho}{4}\right)^2 - \left(\frac{\beta\rho}{4}\right)^3}{\left(1 - \frac{\beta\rho}{4}\right)^3} - \alpha\rho^2, \tag{33}$$

where G no longer controls the interaction strength and is set to $G = -1$, and T is the effective temperature. R, α, and β are constants, discussed further in Sec. V. Exact thermodynamic consistency cannot be achieved with this equation of state, however it can be approximated with the correct choice of ϵ [17]. The exact value of ϵ is dependent on the parameters in Eq. (33), which is discussed further in the following, however it is found to approach 2 in the limit of a large density ratio. This is why the method of Guo gives very large errors in gas density, even at a low density ratio. The exact difference method, however, is not fixed to $\epsilon = 0$ but is dependent on ψ^2/ρ, and in fact it gives a value of ϵ greater than 1 but less than 2. It is not our intention to go into this in detail, but merely to point out that because of this the EDM gives significantly better results for the coexistence curve than the method of Guo for this equation of state (and others of a similar form). This has led to the conclusion that the EDM is an improvement over the method of Guo [16], but this is not necessarily the case.

While it is not possible to achieve exact thermodynamic consistency with the Carnahan-Starling equation of state, a very good approximation can be made. The second velocity moment of F_i, Eq. (A11), can be chosen such that $\gamma(\tau)$ is given by

$$\gamma = 1 - \frac{1}{4\tau} - \frac{\rho}{G c_s^2 \psi^2 \tau}\frac{\epsilon_0}{8} \tag{34}$$

rearranging Eq. (28) for the specific case of $\lambda = 1/6$, and using $c_s^2 = 1/3$. An approximation for ϵ_0 can be found by solving Eq. (14) for a general value of ϵ and setting this equal to the pseudopotential in Eq. (32). This gives

$$\left(\frac{\rho}{\epsilon_0}\right)^{1/\epsilon_0} \propto \sqrt{\frac{2\left[p_0(\rho) - \rho c_s^2\right]}{G c_s^2}} \tag{35}$$

for $\rho = \rho_g$ and $\rho = \rho_l$. While in general this cannot be solved exactly, an approximation for ϵ_0 can be found by an iterative procedure. For high density ratios, ϵ is found to be very close to 2, therefore solving for ϵ_0 can be avoided and $\epsilon_0 = 2$ can be used without a significant loss of accuracy. The results for this forcing scheme are given in Sec. V. For now it should be stressed that while previous methods have proposed improved coexistence curves by introducing a tunable parameter (see, for example, Refs. [16,17]), this is not the case here. For example, Kupershtokh *et al.* [16] used a combination of two different discretization schemes for F_i, and they tuned the weighting of each scheme to improve the recovery of the coexistence curve. The discretization schemes differ in their higher-order error terms, and this tuning is effectively a tuning of these errors to reproduce the required value of ϵ. Here no tuning is required, but an approximation to ϵ is needed to counteract the inherent thermodynamic inconsistency of the pseudopotential model.

IV. SURFACE TENSION

The new terms identified in the pressure tensor affect the surface tension. To be able to control surface tension, further terms should be included in the second moment of F_i. The expression for γ will then have to be modified such that ϵ is unaffected by these new terms. We define $\mathbf{\Theta}$ as the new term in the second moment of F_i, and we write the general form of the forcing term as

$$F_i = w_i\left[\frac{(\mathbf{v}_i - \mathbf{u})\cdot\mathbf{F}}{c_s^2} + \frac{(\mathbf{v}_i\cdot\mathbf{u})(\mathbf{v}_i\cdot\mathbf{F})}{c_s^4} + \gamma\left(\frac{(\mathbf{v}_i\cdot\mathbf{F})^2}{2c_s^4\rho} - \frac{\mathbf{F}\cdot\mathbf{F}}{2c_s^2\rho}\right) + \frac{\left(\mathbf{v}_i\mathbf{v}_i - c_s^2\mathbf{I}\right)\cdot\mathbf{\Theta}}{2\tau c_s^4}\right]. \tag{36}$$

With this definition, the zeroth and first moments of F_i, Eq. (4), are unchanged, and the second moment becomes

$$\mathbf{\Psi} = (\mathbf{Fu} + \mathbf{uF}) + \gamma(\tau)\frac{\mathbf{FF}}{\rho} + \frac{1}{\tau}\mathbf{\Theta}. \tag{37}$$

We then define $\mathbf{\Theta}$ to be

$$\mathbf{\Theta} = Gc_s^2\psi\left[-\frac{\kappa}{2}\sum_i w_i[\psi(\mathbf{x}+\mathbf{v}_i)-\psi(\mathbf{x})]\mathbf{v}_i\mathbf{v}_i + \frac{\kappa+1}{12}\mathbf{I}\sum_i w_i[\psi(\mathbf{x}+\mathbf{v}_i)-2\psi(\mathbf{x})+\psi(\mathbf{x}-\mathbf{v}_i)]\right], \tag{38}$$

as proposed by Li and Luo [25] but with an additional term to account for the higher-order error terms identified here. This results in the pressure tensor being

$$\begin{aligned}\mathbf{P} = &\left[\rho c_s^2 + G\frac{c_s^2}{2}\psi^2 + \frac{Gc_s^2}{2}\left(\lambda+\frac{1}{18}\right)|\nabla\psi|^2 + Gc_s^2\left(\lambda+\frac{1}{18}\right)\psi\mathbf{\Delta}\psi\right]\mathbf{I}\\ &+ Gc_s^2\left[-\lambda+\frac{c_s^2}{6}-Gc_s^2\left(\tau-\frac{1}{4}-\tau\gamma\right)\frac{\psi^2}{\rho}\right]\nabla\psi\nabla\psi\\ &+ Gc_s^2\left(\frac{c_s^2}{6}-\frac{\kappa}{18}\right)\psi\nabla\nabla\psi.\end{aligned} \tag{39}$$

With this modification, and again taking the specific case of $\lambda = 1/6$, γ should now be

$$\gamma = 1 - \frac{1}{4\tau} - \left(\frac{5-\kappa}{36}\right)\frac{\rho\epsilon_0}{Gc_s^2\psi^2\tau}. \tag{40}$$

With this pressure tensor and the expression for γ, the surface tension can be found using Eq. (15) to be

$$\sigma = -Gc_s^2\sigma_c\int_{-\infty}^{\infty}\left|\frac{\partial\psi}{\partial x}\right|^2 dx, \tag{41}$$

where

$$\frac{\partial}{\partial x}\left(\psi\frac{\partial\psi}{\partial x}\right) = \psi\frac{\partial^2\psi}{\partial x^2} + \left(\frac{\partial\psi}{\partial x}\right)^2 \tag{42}$$

has been used, and the surface tension coefficient is given by

$$\sigma_c = \frac{\kappa}{18} - \frac{1}{6} + \epsilon_0\left(\frac{\kappa-5}{36}\right). \tag{43}$$

Surface tension can now be controlled by varying κ, while the modification to γ should allow surface tension to be varied without affecting the liquid and gas densities. Results for this are given in the following section.

It is also important to be able to vary the width of the diffusive interface without changing other properties of the model. For the Carnahan-Starling equation of state, we set $R = \alpha$, and increasing α will decrease the number of lattice points in the interface. A relationship for the width of the interface can be found following Jacqmin [26]. Using Eq. (40), the pressure normal to a flat interface with gradients only in the x direction is given by

$$P_{xx} = \rho c_s^2 + G\frac{c_s^2}{2}\psi^2 - Gc_s^2\left(\frac{5-\kappa}{36}\epsilon_0\right)\left(\frac{\partial\psi}{\partial x}\right)^2 + Gc_s^2\left(\frac{5-\kappa}{18}\right)\psi\frac{\partial^2\psi}{\partial x^2}, \tag{44}$$

from which an approximation to the interface width can be found as

$$W \propto \sqrt{\frac{5-\kappa}{\alpha}\epsilon_0}, \tag{45}$$

where W is a measure of the width of the diffusive interface, in lattice units. (As with all diffusive interface methods, it should be noted that the numerical interface widths are orders of magnitude larger than the physical interfaces.) This is only an approximation due to the inexact thermodynamic consistency, but, as results show, it allows for control of the interface width with very little error. Surface tension is proportional to the coefficient given above, σ_c, and the reciprocal of this interface width. By varying κ and α, and taking into account the required variation of ϵ_0 with varying κ, it is therefore possible to vary both surface tension and interface width independently, without effecting the liquid and gas densities. It has been a long-standing criticism of the interaction potential multiphase LBM that such independent variation of model parameters was not possible, although it should be noted that other multiphase lattice Boltzmann models, such as that proposed by Lee and Fischer [27], have introduced separate parameters for tuning the interface width and the surface tension. While previous work by Sbragaglia *et al.* [13] appeared to relax the constraint on independent tuning of the surface tension and the density ratio for the interaction potential model, it was shown recently that changing the surface tension with the additional parameter introduced in their model still results in small changes in the density ratio [28]. This is likely due to the neglect of the higher-order terms discussed here, and it will be considered in future work.

V. RESULTS

In the following, we present the results for the forcing scheme for the multiphase LBM described above. First, results for improved reproduction of the coexistence curve in one dimension are given. The effect of varying the surface tension parameter and the interface width are then considered in one dimension to ensure that the newly introduced control of the surface tension does not effect the result for improved reproduction of liquid and gas densities. Droplets in two dimensions are then considered, including the impact of the new surface tension coefficient on the measured surface tension, and the effect of varying the interface width on the spurious velocities found around curved phase boundaries.

A. Coexistence curve

As an example, Fig. 1 shows the coexistence curves obtained with the method of Guo *et al.* [15], the EDM, and the present method for the exponential form of the equation of state, compared with the result from the Maxwell equal area

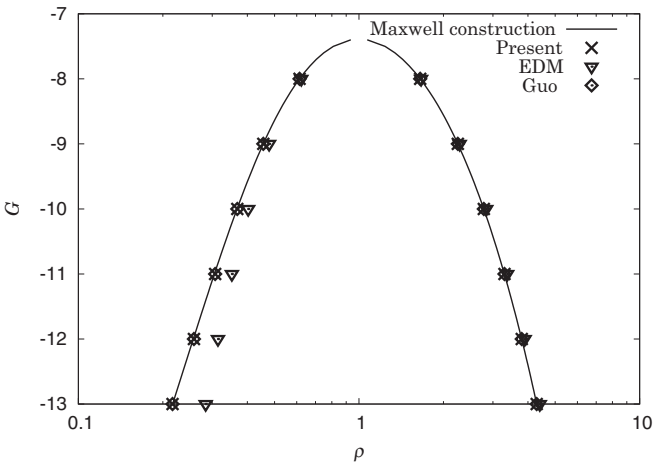

FIG. 1. Simulation results for gas densities in one dimension, for $\psi = \exp(-1/\rho)$. The method of Guo (diamonds), the EDM (triangles), and the present method (crosses) are shown compared with the Maxwell construction (black line).

construction. For this specific case, as described in Sec. III, the method of Guo agrees exactly with the present method with $\epsilon_0 = 0$, and both are seen to be in good agreement with the coexistence curve. As expected, the EDM gives errors in the vapor branch. This equation of state is not discussed further; the following results will focus on the Carnahan-Starling equation of state. Figure 2 shows the coexistence curves obtained with the method of Guo *et al.* [15] and the EDM, for the Carnahan-Starling equation of state, compared with the result from the Maxwell equal area construction. In all schemes, the liquid density only shows a small variation across the different forcing schemes, therefore only the vapor phase results are shown. Both Guo's scheme and the EDM are shown

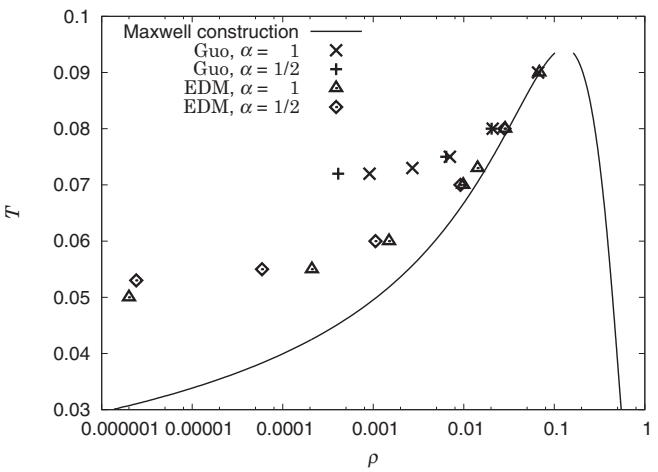

FIG. 2. Simulation results for gas densities in one dimension, for the Carnahan-Starling equation of state. The method of Guo with $\alpha = 1$ (crosses) and $\alpha = 1/2$ (pluses) and the EDM with $\alpha = 1$ (triangles) and $\alpha = 1/2$ (diamonds) are shown compared with the Maxwell construction (black line). In both cases, increasing the interface width (by decreasing α) does not improve the results. (Liquid densities are all in close agreement with the Maxwell construction and are therefore not shown.)

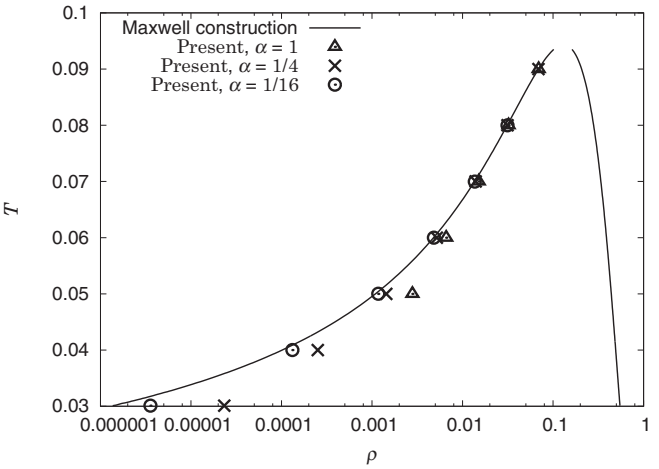

FIG. 3. Simulation results for gas densities in one dimension, for the Carnahan-Starling equation of state. The present method with increasing interface widths, using $\alpha = 1$ (triangles), $\alpha = 1/4$ (crosses), and $\alpha = 1/16$ (circles), is shown compared with the Maxwell construction (black line). $\alpha = 1$, $1/4$, and $1/16$ give interface widths of, for example, $W = 3.0, 5.8$, and 11.5, respectively, at $T = 0.07$, reducing to $W = 3.2$ and 6.1 for $\alpha = 1/4$ and $1/16$ at $T = 0.04$ (at which point the interface width at $\alpha = 1$ has become too small for a stable solution). Significant improvement over existing methods (shown in Fig. 2) is observed, with results tending to the correct density with increasing interface width (decreasing α). (Liquid densities are all in close agreement with the Maxwell construction and are therefore not shown.)

using $\alpha = 1$. Increasing the interface widths by decreasing α was found to give worse results in both cases, as is also shown for $\alpha = 1/2$. It can be seen that Guo's method does not agree with the Maxwell construction, even at relatively low density ratios, and that while the EDM improves on this, it also shows significant errors as the density ratio is increased. This is in agreement with the result of Kupershtokh *et al.* [16], however the improvement of the EDM is a coincidental result of error terms increasing ϵ so as to give a better approximation of thermodynamic consistency. As discussed above, for the nine velocity stencil in the forcing calculation, Eq. (5), Guo's method gives $\epsilon = 0$, whereas for approximate thermodynamic consistency with the Carnahan-Starling equation of state, ϵ is found to tend toward 2.

The results for the present method using γ given by Eq. (34) are shown in Fig. 3. For each point, an approximate value for ϵ_0 is found, as described above. This ranged from 1.87 for the lowest density ratio (at $T = 0.09$) to 2 for most of the higher density ratio cases. It should be stressed again that the approximations for ϵ_0 are found by comparing ψ from Eq. (32) with ψ from the general solution of Eq. (14), and not by tuning ϵ until the coexistence curve is correct. Three values of α are given ($\alpha = 1$, $1/4$, and $1/16$), showing results for increasingly wider interfaces. It can be seen that the coexistence curve from the present method is in very good agreement with the Maxwell construction, and that this improvement increases systematically with increasing interface width. All density ratios can be reproduced accurately, as long as the interface is wide enough. We proceed by quantifying this for a few specific cases.

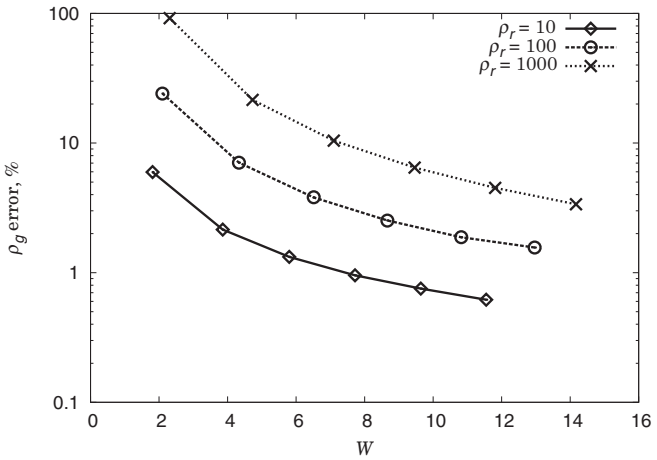

FIG. 4. Error in gas density (compared with the predicted gas density from the Maxwell construction) with interface width, W, for the present forcing scheme with the Carnahan-Starling equation of state. Three different density ratios are shown: $\rho_r \approx 10$ using $T = 0.0790$ (diamonds, solid line), $\rho_r \approx 100$ using $T = 0.0585$ (circles, dashed line), and $\rho_r \approx 1000$ using $T = 0.0455$ (crosses, dotted line).

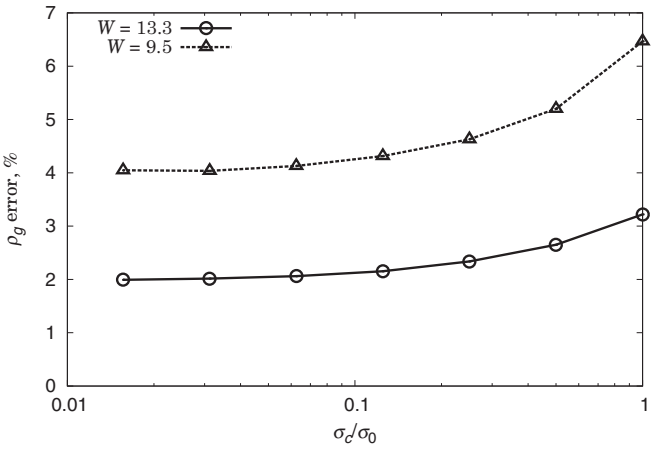

FIG. 5. Error in gas density (compared with the predicted gas density from the Maxwell construction) with varying surface tension parameter, σ_c, for the present forcing scheme. The result is for the Carnahan-Starling equation of state with $T = 0.0455$ (density ratio of approximately 1000). σ_0 is σ_c with $\kappa = 0$. Two different interface widths are shown: $W = 9.5$ (triangles, dashed line) and $W = 13.3$ (circles, solid line).

The interface width, W, is measured by fitting the following curve to the density distribution across an interface:

$$\rho(x) = \frac{\rho_l + \rho_g}{2} + \frac{\rho_l - \rho_g}{2} \tanh\left(\frac{2x}{W}\right). \tag{46}$$

Although it should be noted that the interface does not exactly follow this function, it is a good approximation. For three different density ratios, the interface width was varied between approximately $W = 2$ and 14 lattice units. This was achieved by simultaneously varying κ and α so as to vary the interface width while keeping the surface tension constant (measurements of surface tension are deferred to the following section). Three effective temperatures were used in the Carnahan-Starling equation of state ($T = 0.0790$, 0.0585, and 0.0455) to give predicted density ratios, ρ_r, of approximately 10, 100, and 1000, respectively. Figure 4 shows the percentage difference between the predicted gas density and the gas density measured from simulation (of a flat interface on a 450×5 grid, run to equilibrium) for the three effective temperatures. As discussed above, the difference between the gas density from the simulation result and the Maxwell construction reduces with increased interface width. This is seen to happen at the same rate for all interface widths. The worst result shows a gas density twice that of the predicted density; this is at a large density ratio and a very small interface width. It is also significantly better than the error in the EDM, which gives gas densities orders of magnitude below the correct densities at $T = 0.05$. The observed systematic reduction in error as the high gradients at the interface are spread out over more lattice sites may appear trivial, but it should be reiterated that for the previous forcing schemes, increasing the interface width resulted in larger errors. This has previously made mesh refinement difficult in the pseudopotential multiphase LBM, a major obstacle that the present method overcomes.

Having introduced a parameter for varying the surface tension and discussed varying the interface width in the preceding section, it is important to ensure that varying this surface tension parameter does not effect the densities or the interface width. For an effective temperature of $T = 0.0455$ (a density ratio of approximately 1000), Fig. 5 shows the change in the gas density error for reducing the surface tension parameter over a large range. For both interface widths shown, very little change in gas density is observed, with the error reducing slightly as the surface tension parameter is reduced (measurements of surface tension with varying surface tension parameter are given in the following section). The interface widths also show very little variation, from 9.46 to 9.38 lattice units in the first case, and from 13.33 to 13.28 in the second. Even for this high density ratio case, the surface tension parameter can be varied with negligible effects on both gas density and interface width.

B. Surface tension

Having established that the surface tension parameter, σ_c, can be varied with only slight effects on the gas density, and that increasing the interface width decreases error in the gas density, we now consider surface tension. First varying surface tension at a fixed interface width is investigated, followed by varying the interface width at a fixed surface tension. In both cases, in addition to measuring the interface width, using Eq. (46) and surface tension, the average spurious velocity magnitude and the isotropy were also measured. Isotropy is defined as

$$I = \left| \frac{r_0}{r_{45}} - 1 \right|, \tag{47}$$

where r is the radius of the droplet, and the subscripts indicate the angle to the x axis of the line along which the radius is measured (radii being measured at the density midpoint in the

diffusive interface). Surface tension was measured using both the Laplace law and an oscillating droplet. In two dimensions, the Laplace law is given by

$$\Delta P = \frac{\sigma}{r}, \tag{48}$$

where ΔP is the pressure difference between the inside and outside of the droplet. For a droplet centered at (x_0, y_0) given an initial velocity

$$u_x = U_0 \frac{x - x_0}{r}, \quad u_y = -2U_0 \frac{y - y_0}{r}, \tag{49}$$

under the assumption that the viscosities in the liquid and gas phase are sufficiently small, and that deviations of the interface from equilibrium are small compared to the droplet radius, the surface tension is related to the frequency of oscillation, Ω, by [29]

$$\sigma = \frac{(\rho_l + \rho_g) r^3}{6\Omega^2}. \tag{50}$$

To measure surface tension using the Laplace law, droplets of radius between 20 and 50 were initiated in the center of a 250×250 domain. Once equilibrium was reached, the liquid and gas densities and the radius were measured. The pressure difference, ΔP, is then plotted against $1/r$ and the surface tension obtained from the gradient of a linear fit. For measurements using the oscillating droplet, a droplet of radius 40 was initiated in the center of a 500×500 domain. Once equilibrium was reached, the liquid and gas densities and the radius were again measured, and an initial velocity, given by Eq. (49), was applied, with U_0 kept small enough such that the maximum amplitude of oscillations was less than 10% of the droplet radius. The oscillation period was then measured over at least five oscillations.

To investigate varying surface tension at a fixed interface width, the Carnahan-Starling equation of state is used with $T = 0.0585$ and 0.0455, giving density ratios (over a flat interface) of 100 and 1000, respectively. By simultaneously varying κ and α, the interface width can be kept constant, by Eq. (45), and the surface tension reduced, by Eq. (43) and using $\sigma \propto \sigma_c / W$. As α is varied, a new fit for ϵ_0 is required, in most cases $\epsilon_0 \approx 2$. For all results $\tau = 1$, different relaxation times were tested for a number of cases with virtually no effect on the density ratio or the surface tension (the slight variations being due to increases in spurious velocities as the viscosity is decreased). At each temperature, two interface widths were used. For $T = 0.0585$ and 0.0455, the initial cases (corresponding to no reduction in surface tension using the present method, with $\kappa = 0$) were $\alpha = 0.125$ and 0.0625, and $\alpha = 0.031\,25$ and 0.015 625, respectively. Measured interface widths for each of the four cases were $W = 6.1$, 8.7, 9.4, and 13.3. Small increases in interface widths were observed as surface tension was decreased. At a 32-fold theoretical reduction in surface tension, the four widths were $W = 6.3$, 9.2, 9.9, and 14.2. The Laplace law for the first case is shown in Fig. 6, with results for successively quartering the theoretical surface tension. Linear fits are in good agreement, except for the well-known offset from the origin. Figure 7 shows the corresponding measured values of surface tension. Also shown are measured values for the second case. In both

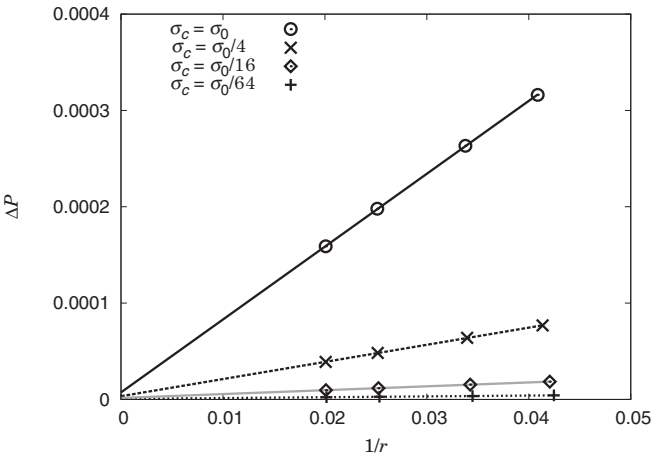

FIG. 6. Laplace law results for $T = 0.0585$ giving a density ratio of approximately 100 and an interface width of $W = 6.1$, including linear fits. Theoretical surface tensions (normalized by surface tension at $\kappa = 0$, σ_0) are 1 (circles, solid black line), 1/4 (crosses, dashed line), 1/16 (diamonds, solid gray line), and 1/64 (pluses, dotted line).

cases, a linear reduction in measured surface tension with theoretical surface tension is observed. It is of particular note that this is true even at low values of surface tension. Figure 8 shows the two results at $T = 0.0455$; again, the correct linear relationship is observed, even at low surface tension. Certain values of surface tension were measured using the oscillating droplet. In those cases, $\tau = 0.59$ was used as a compromise between stability and the low viscosity approximation in the relationship between oscillation frequency and surface tension. Only slight deviations between these measurements and those from the Laplace law were recorded, with the largest being approximately 10% for a low surface tension case. Results are also plotted in Fig. 8 and show good agreement with the Laplace law results.

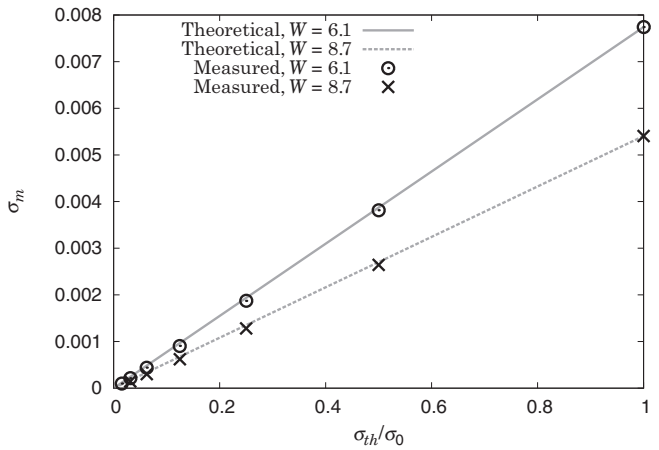

FIG. 7. Measured surface tension, σ_m, against theoretical surface tension σ_{th} (normalized by surface tension at $\kappa = 0$, σ_0). $T = 0.0585$ giving $\rho_r \approx 100$. Results shown are for measurements made using the Laplace law, for two fixed interface widths: $W = 6.1$ (circles) and $W = 8.7$ (crosses). Solid and dashed lines show the theoretical linear relationship, with gradient equal to σ_0 for each case.

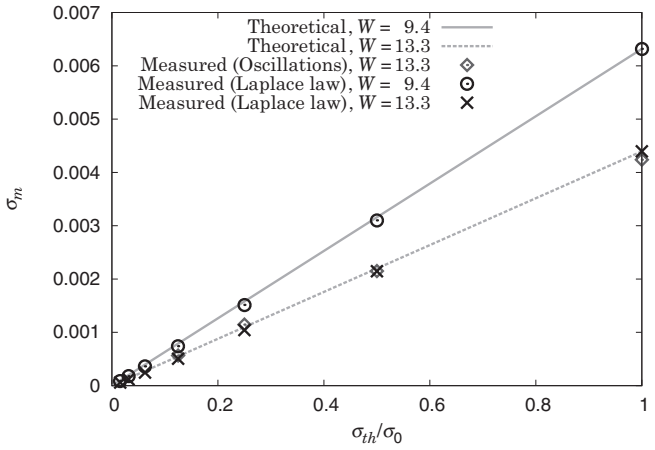

FIG. 8. Measured surface tension, σ_m, against theoretical surface tension σ_{th} (normalized by surface tension at $\kappa = 0$, σ_0). $T = 0.0455$ giving $\rho_r \approx 1000$. Results shown are for measurements made using the Laplace law, for two fixed interface widths: $W = 9.4$ (circles) and $W = 13.3$ (crosses). Also shown for the $W = 13.3$ case are measurements made using oscillating droplets (diamonds). Solid and dashed lines show the theoretical linear relationship, with gradient equal to σ_0 for each case.

Figures 9 and 10 show variation in the spurious velocity and isotropy for each of the two cases for $T = 0.0585$ and 0.0455, respectively. In all cases, anisotropy increases as surface tension is decreased, however this increase becomes more gradual toward lower surface tension. It is also lower for wider interfaces; additional results in that regard are given below. Spurious velocities, however, are seen to decrease slightly as surface tension is decreased.

C. Interface width

We now consider varying the interface width at a fixed surface tension, again using the same two density ratios. In each case, two surface tensions were used: $\sigma = 0.0077$ and 0.000 91, and $\sigma = 0.0063$ and 0.000 74, respectively. In all cases, measured interface widths were in very good agreement with theoretical values. In the worst case, with $\rho_r = 1000$ and $\sigma = 0.000\,74$, a theoretical factor of 6 between the largest and smallest interface widths gave a measured factor of 6.4 (the largest and smallest interfaces having $W = 14.7$ and 2.3, respectively). In all cases, interface widths were increased to values above 10 and decreased to the lowest stable value. This was found to be around 2 or 3. Variation in surface tension was found to be less than a few percent everywhere except for at the lowest interface widths.

Figures 11 and 12 show the variation in spurious velocities and isotropy with measured interface width for each of the two

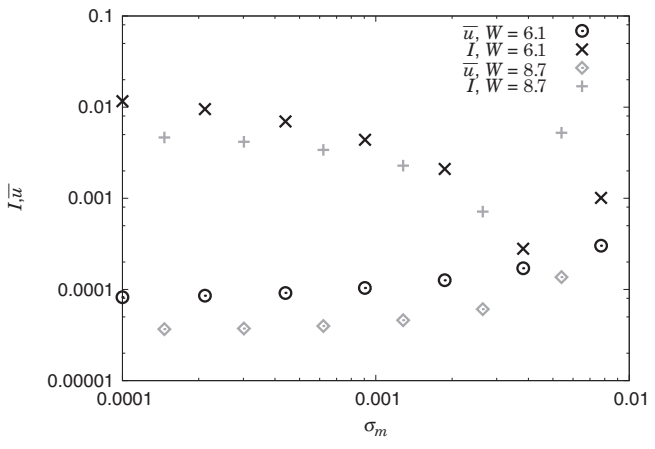

FIG. 9. Variation in isotropy, I, defined in Eq. (47), and average spurious velocity, $\bar{u}$, with measured surface tension, σ_m. $T = 0.0585$ giving $\rho_r \approx 100$. Results for isotropy (crosses) and spurious velocity (circles) in black are for an interface width of $W = 6.1$. Results for isotropy (pluses) and spurious velocity (diamonds) in grey are for an interface width of $W = 8.7$.

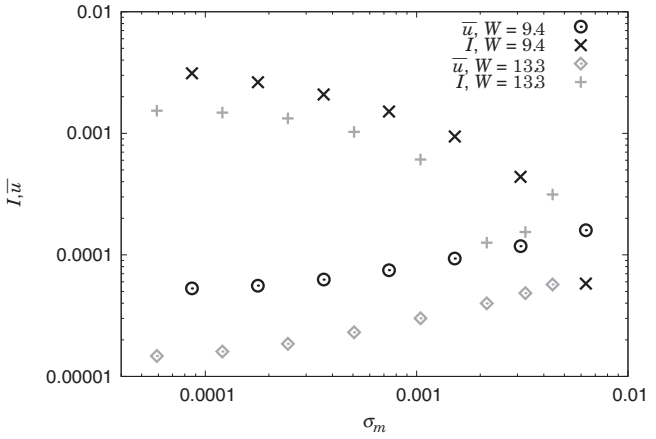

FIG. 10. Variation in isotropy, I, defined in Eq. (47), and average spurious velocity, $\bar{u}$, with measured surface tension, σ_m. $T = 0.0455$ giving $\rho_r \approx 1000$. Results for isotropy (crosses) and spurious velocity (circles) in black are for an interface width of $W = 9.4$. Results for isotropy (pluses) and spurious velocity (diamonds) in gray are for an interface width of $W = 13.3$.

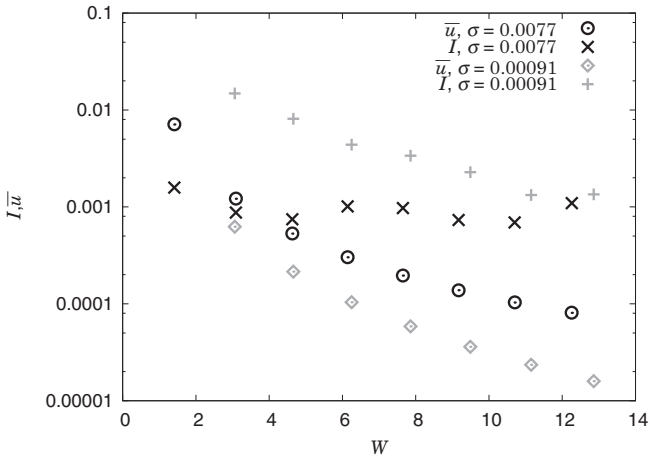

FIG. 11. Variation in isotropy, I, defined in Eq. (47), and average spurious velocity, $\bar{u}$, with measured interface width, W. $T = 0.0585$ giving $\rho_r \approx 100$. Results for isotropy (crosses) and spurious velocity (circles) in black are for a surface tension of $\sigma = 0.0077$. Results for isotropy (pluses) and spurious velocity (diamonds) in gray are for a surface tension of $\sigma = 0.000\,91$.

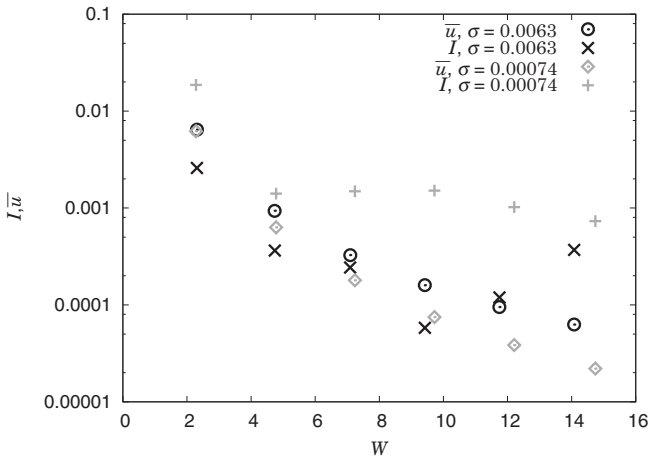

FIG. 12. Variation in isotropy, I, defined in Eq. (47), and average spurious velocity, $\bar{u}$, with measured interface width, W. $T = 0.0455$ giving $\rho_r \approx 1000$. Results for isotropy (crosses) and spurious velocity (circles) in black are for a surface tension of $\sigma = 0.0063$. Results for isotropy (pluses) and spurious velocity (diamonds) in gray are for a surface tension of $\sigma = 0.000\,74$.

cases for $T = 0.0585$ and 0.0455, respectively. In all cases, the average spurious velocity is found to reduce with increasing interface width. In general, anisotropy is also seen to decrease with increasing interface width. While this relationship is not exact, anisotropy is small except for at the smallest interface widths, which in practice would not be used. Spurious velocities are seen to be converging to zero at a rate of between $1/W^2$ and $1/W^3$, with the exact rate having some dependence on the density ratio and surface tension. Having shown that interface width can be varied without significantly effecting the density ratio and surface tension, this allows systematic control over spurious velocities. This has not previously been possible with the pseudopotential multiphase LBM. However, it should be noted that the width of the diffusive interface, W, should be kept small compared with the relevant length scale of the system being studied. The ability to control interface width without affecting the density ratio and surface tension is also important for mesh refinement, which is a basic requirement for any CFD methodology. As the interface width has not been independently controllable in the previous pseudopotential models, it has not been possible to show convergence as the number of lattice points in the interface is increased. The present method, therefore, represents a major step toward the LBM becoming a superior simulation tool for real-world multiphase flow applications.

VI. CONCLUSION

A third-order analysis has identified the errors in the pressure tensor in the pseudopotential lattice Boltzmann method (LBM). As a result, an improved forcing scheme has been proposed, which enables the full range of coexistence curves to be accurately reproduced, even at arbitrarily high density ratios (at the cost of increasing interface width, and therefore increased computational cost in keeping the relative interface width constant). Moreover, the addition of a term to the pseudopotential method allows variation of surface tension over a wide range, independent of the density ratio. Interface width can also be varied independently of density ratio and surface tension. Increasing the interface width enables a systematic reduction of errors, leading to an orders-of-magnitude reduction in the level of spurious currents at the interfaces. Furthermore, the ability to independently tune the interface width allows mesh refinement studies, which up until now has been unavailable to the pseudopotential method, despite being vital to any CFD methodology. In summary, these developments enable the pseudopotential LBM to tackle multiphase flow problems in real-world applications. The above higher-order analysis of the forcing term is general, so the findings of this study are not confined to the pseudopotential LBM method considered here. The improved forcing term treatment, therefore, can be used in conjunction with other enhancements to the LBM. For example, the present investigation uses a single-relaxation-time model, but the derivation given here could be extended for multiple-relaxation-time models. Further work will demonstrate the full capabilities of the proposed LBM methodology and its applications in a variety of multiphase phenomena.

ACKNOWLEDGMENT

Support is acknowledged from the UK Consortium on Mesoscale Engineering Sciences (UKCOMES) under EPSRC Grant No. EP/L00030X/1.

APPENDIX

Starting from Eq. (21), the equations for the conservation of mass and momentum, Eqs. (22) and (24), are derived. The zeroth and first velocity moments of Eq. (21) result in

$$\begin{aligned}\frac{\partial\rho}{\partial t}+\nabla\cdot(\rho\mathbf{u}) &= \left(\tau-\frac{1}{2}\right)\left[\frac{\partial^2\rho}{\partial t^2}+2\frac{\partial}{\partial t}\nabla\cdot(\rho\mathbf{u})+\nabla\cdot\left(\nabla\cdot\mathbf{\Pi}^0\right)\right]\\ &+\left(-\tau^2+\tau-\frac{1}{6}\right)\left[\frac{\partial^3\rho}{\partial t^3}+3\frac{\partial^2}{\partial t^2}\nabla\cdot(\rho\mathbf{u})+3\frac{\partial}{\partial t}\nabla\cdot(\nabla\cdot\mathbf{\Pi}^0)+\nabla\cdot(\nabla\cdot(\nabla\cdot\mathbf{Q}^0))\right]\\ &-\tau\nabla\cdot\mathbf{F}+\tau\left(\tau-\frac{1}{2}\right)\left[2\frac{\partial}{\partial t}\nabla\cdot\mathbf{F}+\nabla\cdot(\nabla\cdot\mathbf{\Psi})\right]\\ &+\tau\left(-\tau^2+\tau-\frac{1}{6}\right)\left[3\frac{\partial^2}{\partial t^2}\nabla\cdot\mathbf{F}+3\frac{\partial}{\partial t}\nabla\cdot(\nabla\cdot\mathbf{\Psi})+\nabla\cdot(\nabla\cdot(\nabla\cdot\mathbf{\Xi}))\right]\end{aligned} \tag{A1}$$

and

$$\begin{aligned}\frac{\partial}{\partial t}(\rho\mathbf{u})+\nabla\cdot\mathbf{\Pi}^0=&\left(\tau-\frac{1}{2}\right)\left[\frac{\partial^2}{\partial t^2}(\rho\mathbf{u})+2\frac{\partial}{\partial t}\nabla\cdot\mathbf{\Pi}^0+\nabla\cdot(\nabla\cdot\mathbf{Q}^0)\right]\\&+\left(-\tau^2+\tau-\frac{1}{6}\right)\left[\frac{\partial^3}{\partial t^3}(\rho\mathbf{u})+3\frac{\partial^2}{\partial t^2}\nabla\cdot\mathbf{\Pi}^0+3\frac{\partial}{\partial t}\nabla\cdot(\nabla\cdot\mathbf{Q}^0)+\nabla\cdot(\nabla\cdot(\nabla\cdot\mathbf{A}^0))\right]\\&+\mathbf{F}-\tau\left(\frac{\partial}{\partial t}\mathbf{F}+\nabla\cdot\mathbf{\Psi}\right)+\tau\left(\tau-\frac{1}{2}\right)\left[\frac{\partial^2}{\partial t^2}\mathbf{F}+2\frac{\partial}{\partial t}\nabla\cdot\mathbf{\Psi}+\nabla\cdot(\nabla\cdot\mathbf{\Xi})\right]\\&+\tau\left(-\tau^2+\tau-\frac{1}{6}\right)\left[\frac{\partial^3}{\partial t^3}\mathbf{F}+3\frac{\partial^2}{\partial t^2}\nabla\cdot\mathbf{\Psi}+3\frac{\partial}{\partial t}\nabla\cdot(\nabla\cdot\mathbf{\Xi})\right].\end{aligned}\tag{A2}$$

The first and second differentials with respect to time of the momentum equation are then used recursively to eliminate terms in that equation. Similarly, the first and second differentials with respect to time of the mass equation, along with the divergence of the resulting momentum equation, are used to eliminate terms in the mass equation, resulting in the familiar equation for the conservation of mass,

$$\frac{\partial\rho}{\partial t}+\nabla\cdot(\rho\tilde{\mathbf{u}})=0.\tag{A3}$$

The fluid velocity is now defined to take into account the additional terms in the conservation of mass equation that result from the higher-order expansion:

$$\rho\tilde{\mathbf{u}}=\rho\mathbf{u}+\frac{1}{2}\mathbf{F}-\frac{1}{12}\frac{\partial}{\partial t}\nabla\cdot\mathbf{\Pi}^0-\frac{1}{12}\nabla\cdot(\nabla\cdot\mathbf{Q}^0)-\frac{1}{6}\frac{\partial}{\partial t}\mathbf{F}-\frac{1}{24}\frac{\partial^2}{\partial t^2}\mathbf{F}-\left(-\tau^3+\frac{\tau}{2}\right)\frac{\partial}{\partial t}\nabla\cdot(\nabla\cdot\mathbf{\Psi})-\frac{\tau}{12}\nabla\cdot(\nabla\cdot\mathbf{\Xi}).\tag{A4}$$

Using this definition of fluid velocity, the conservation of momentum is now given by

$$\begin{aligned}\frac{\partial}{\partial t}(\rho\tilde{\mathbf{u}})+\nabla\cdot\mathbf{\Pi}^0=&\left(\tau-\frac{1}{2}\right)\left[\frac{\partial}{\partial t}\nabla\cdot\mathbf{\Pi}^0+\nabla\cdot(\nabla\cdot\mathbf{Q}^0)\right]+\mathbf{F}-\tau\nabla\cdot\mathbf{\Psi}+\left(-\tau^2+\tau-\frac{1}{6}\right)\frac{\partial^2}{\partial t^2}\nabla\cdot\mathbf{\Pi}^0\\&+\left(-2\tau^2+2\tau-\frac{1}{3}\right)\frac{\partial}{\partial t}\nabla\cdot(\nabla\cdot\mathbf{Q}^0)+\left(-\tau^2+\tau-\frac{1}{6}\right)\nabla\cdot(\nabla\cdot(\nabla\cdot\mathbf{A}^0))\\&+\left(\tau^2-\frac{\tau}{2}\right)\left[\frac{\partial}{\partial t}\nabla\cdot\mathbf{\Psi}+\nabla\cdot(\nabla\cdot\mathbf{\Xi})\right].\end{aligned}\tag{A5}$$

Third-order derivatives of moments of $\mathbf{F}$ have been dropped, and derivatives in time of $\mathbf{F}$ have been assumed much smaller than derivatives in space (this assumption would become invalid in the presence of an oscillatory driving force above a certain frequency, but it is acceptable for the multiphase forcing terms considered here). The first three terms on the right-hand side are captured by the usual second-order expansion techniques and are therefore treated in the literature, and up to the order considered here the first term contains

$$\frac{\partial}{\partial t}\mathbf{\Pi}^0+\nabla\cdot\mathbf{Q}^0=T_0\rho[\nabla\mathbf{u}+(\nabla\mathbf{u})^{\mathrm{T}}]+(\mathbf{F}\mathbf{u}+\mathbf{u}\mathbf{F})-\frac{T_0}{2}(\nabla\cdot\mathbf{F})\,\mathbf{I},\tag{A6}$$

where $T_0=c_s^2$. Using Eq. (23), this can be rewritten as

$$\frac{\partial}{\partial t}\mathbf{\Pi}^0+\nabla\cdot\mathbf{Q}^0=T_0\rho[\nabla\tilde{\mathbf{u}}+(\nabla\tilde{\mathbf{u}})^{\mathrm{T}}]+(\mathbf{F}\mathbf{u}+\mathbf{u}\mathbf{F})-\frac{T_0}{2}[(\nabla\cdot\mathbf{F})\mathbf{I}+\nabla\mathbf{F}+(\nabla\mathbf{F})^{\mathrm{T}}]+\frac{\mathbf{F}\mathbf{F}}{\rho},\tag{A7}$$

where

$$T_0\nabla\rho=\mathbf{F}\tag{A8}$$

and

$$\frac{\partial u_\alpha}{\partial x_\beta}=\frac{\partial}{\partial x_\beta}\left(\hat{u}_\alpha-\frac{F_\alpha}{2\rho}\right)=\frac{\partial\hat{u}_\alpha}{\partial x_\beta}-\frac{1}{2\rho}\frac{\partial F_\alpha}{\partial x_\beta}+\frac{F_\alpha F_\beta}{2T_0\rho^2}\tag{A9}$$

have been used, both correct at this order.

The new terms in Eq. (A5) require further consideration. The equilibrium values of the moments are replaced by their (lattice-dependent) expressions in terms of ρ, $\mathbf{u}$, and T_0. The derivatives of ρ and $\rho\mathbf{u}$ with respect to time can then be replaced recursively with Eqs. (A3) and (A5). The terms on the right-hand side of Eq. (A5) then contribute the following to $\mathbf{P}$:

$$\begin{aligned}&\frac{\partial^2}{\partial t^2}\mathbf{\Pi}^0=0,\quad\frac{\partial}{\partial t}\nabla\cdot\mathbf{Q}^0=0,\quad\nabla\cdot(\nabla\cdot\mathbf{A}^0)=T_0^2[(\nabla^2\rho)\mathbf{I}+\nabla\nabla\rho+(\nabla\nabla\rho)^{\mathrm{T}}],\\&\frac{\partial}{\partial t}\mathbf{\Psi}=0,\quad\nabla\cdot\mathbf{\Xi}=T_0[(\nabla\cdot\mathbf{F})\mathbf{I}+\nabla\mathbf{F}+(\nabla\mathbf{F})^{\mathrm{T}}]\end{aligned}\tag{A10}$$

(again temporal derivatives of $\mathbf{F}$ are assumed much smaller than spatial derivatives). The second moment of the forcing term is dependent on the forcing scheme used, and for now it is given in the general form

$$\mathbf{\Psi} = \sum \mathbf{v}_i \mathbf{v}_i F_i = (\mathbf{F}\mathbf{u} + \mathbf{u}\mathbf{F}) + \gamma(\tau)\frac{\mathbf{F}\mathbf{F}}{\rho}, \tag{A11}$$

where $\gamma(\tau)$ is a function of τ dependent on the method. Inserting these into Eq. (A5), collecting terms and again making use of Eq. (A8), leads to

$$\frac{\partial}{\partial t}(\rho\tilde{\mathbf{u}}) + \nabla\left(c_s^2\rho\right) + \nabla\cdot(\rho\tilde{\mathbf{u}}\tilde{\mathbf{u}}) = \nabla\cdot\boldsymbol{\tau} + \mathbf{F} + \nabla\cdot\left[\left(\tau - \frac{1}{4} - \tau\gamma\right)\frac{\mathbf{F}\mathbf{F}}{\rho}\right] + \nabla\cdot\left[\frac{T_0}{12}[(\nabla\cdot\mathbf{F})\mathbf{I} + \nabla\mathbf{F} + (\nabla\mathbf{F})^{\mathrm{T}}]\right], \tag{A12}$$

which is the momentum conservation equation given in Eq. (24).

[1] Y. H. Qian, S. Succi, and S. A. Orszag, Annu. Rev. Comp. Phys. **30**, 195 (1995).
[2] S. Chen and G. D. Doolen, Annu. Rev. Fluid Mech. **30**, 329 (1998).
[3] S. Succi, *The Lattice Boltzmann Equation for Fluid Dynamics and Beyond* (Oxford University Press, Oxford, 2001).
[4] M. R. Swift, W. R. Osborn, and J. M. Yeomans, Phys. Rev. Lett. **75**, 830 (1995).
[5] E. Orlandini, M. R. Swift, and J. M. Yeomans, Europhys. Lett. **32**, 463 (1995).
[6] M. R. Swift, E. Orlandini, W. R. Osborn, and J. M. Yeomans, Phys. Rev. E **54**, 5041 (1996).
[7] X. He, X. Shan, and G. D. Doolen, Phys. Rev. E **57**, R13 (1998).
[8] X. He and G. D. Doolen, J. Stat. Phys. **107**, 309 (2002).
[9] L.-S. Luo, Phys. Rev. Lett. **81**, 1618 (1998).
[10] X. Shan and H. Chen, Phys. Rev. E **47**, 1815 (1993).
[11] X. Shan and H. Chen, Phys. Rev. E **49**, 2941 (1994).
[12] X. Shan and G. Doolen, J. Stat. Phys. **81**, 379 (1995).
[13] M. Sbragaglia, R. Benzi, L. Biferale, S. Succi, K. Sugiyama, and F. Toschi, Phys. Rev. E **75**, 026702 (2007).
[14] P. Yuan and L. Schaefer, Phys. Fluids **18**, 042101 (2006).
[15] Z. Guo, C. Zheng, and B. Shi, Phys. Rev. E **65**, 046308 (2002).
[16] A. L. Kupershtokh, D. A. Medvedev, and D. I. Karpov, Comput. Math. Appl. **58**, 965 (2009).
[17] Q. Li, K. H. Luo, and X. J. Li, Phys. Rev. E **86**, 016709 (2012).
[18] D. Lycett-Brown and K. H. Luo, Comput. Math. Appl. **67**, 350 (2014).
[19] A. J. Wagner, Phys. Rev. E **74**, 056703 (2006).
[20] D. J. Holdych, D. R. Noble, J. G. Georgiadis, and R. O. Buckius, J. Comp. Phys. **193**, 595 (2004).
[21] X. Shan, Phys. Rev. E **77**, 066702 (2008).
[22] Q. Li, K. H. Luo, and X. J. Li, Phys. Rev. E **87**, 053301 (2013).
[23] R. Benzi, L. Biferale, M. Sbragaglia, S. Succi, and F. Toschi, Phys. Rev. E **74**, 021509 (2006).
[24] J. S. Rowlinson and B. Widom, *Molecular Theory of Capillarity* (Clarendon, Oxford, 1982).
[25] Q. Li and K. H. Luo, Phys. Rev. E **88**, 053307 (2013).
[26] D. Jacqmin, J. Comp. Phys. **155**, 96 (1999).
[27] T. Lee and P. F. Fischer, Phys. Rev. E **74**, 046709 (2006).
[28] H. Huang, M. Krafczyk, and X. Lu, Phys. Rev. E **84**, 046710 (2011).
[29] H. Lamb, *Hydrodynamics* (Dover, New York, 1932), p. 738.